1-1-2016

Ambient controlled synthesis of advanced core-shell plasmonic Ag@ZnO photocatalysts

Jinyan Xiong
University of Wollongong, jx513@uowmail.edu.au

Qiao Sun
Soochow University, qsun@uow.edu.au

Jun Chen
University of Wollongong, junc@uow.edu.au

Zhen Li
University of Wollongong, zhenl@uow.edu.au

S X. Dou
University of Wollongong, shi@uow.edu.au

Ambient controlled synthesis of advanced core-shell plasmonic Ag@ZnO photocatalysts

Abstract

Plasmonic Ag@ZnO core-shell hybrids, including hetero-nanowires and hetero-nanoparticles, have been synthesized at room temperature for application in photocatalysis. The morphology, size, crystal structure, and composition of the products were investigated by X-ray diffraction, scanning and transmission electron microscopy, X-ray photoelectron spectroscopy, and ultraviolet-visible spectroscopy. It was found the concentration of Zn(NO3)2·6H2O and the amount of water play crucial roles in the formation of Ag@ZnO core-shell hybrids. The resultant Ag@ZnO core-shell hybrids exhibit much higher photocatalytic activity and stability towards degradation of organic contaminants than pure ZnO nanocrystals under solar light irradiation. The one-dimensional (1D) core-shell hetero-nanowires prepared under optimal conditions (i.e. 0.6 M Zn(NO3)2·6H2O and 14.5 mL water) exhibit the best photocatalytic performance. The drastic enhancement in photocatalytic activity over the Ag@ZnO core-shell hybrids, especially the 1D core-shell hetero-nanowires, could be attributed to the synergistic effects of the surface ZnO and Ag nanowire cores with the surface plasmon resonance and the electron sink effect, as well as the unique 1D core-shell nanostructure for efficient mass transfer. The possible mechanism for degradation of rhodamine B (RhB) under solar light irradiation was discussed. This work provides a very convenient chemical route to prepare stable and highly efficient solar light driven plasmonic core-shell Ag@ZnO photocatalysts for cost-effective water purification.

Keywords

controlled, synthesis, advanced, core, shell, plasmonic, ambient, ag, photocatalysts, zno

Disciplines

Engineering | Science and Technology Studies

Publication Details

Xiong, J., Sun, Q., Chen, J., Li, Z. & Dou, S. (2016). Ambient controlled synthesis of advanced core-shell plasmonic Ag@ZnO photocatalysts. CrystEngComm, 18 (10), 1713-1722.

Volume 18 | Number 10 | 14 March 2016 | Pages 1667–1856

CrystEngComm

www.rsc.org/crystengcomm

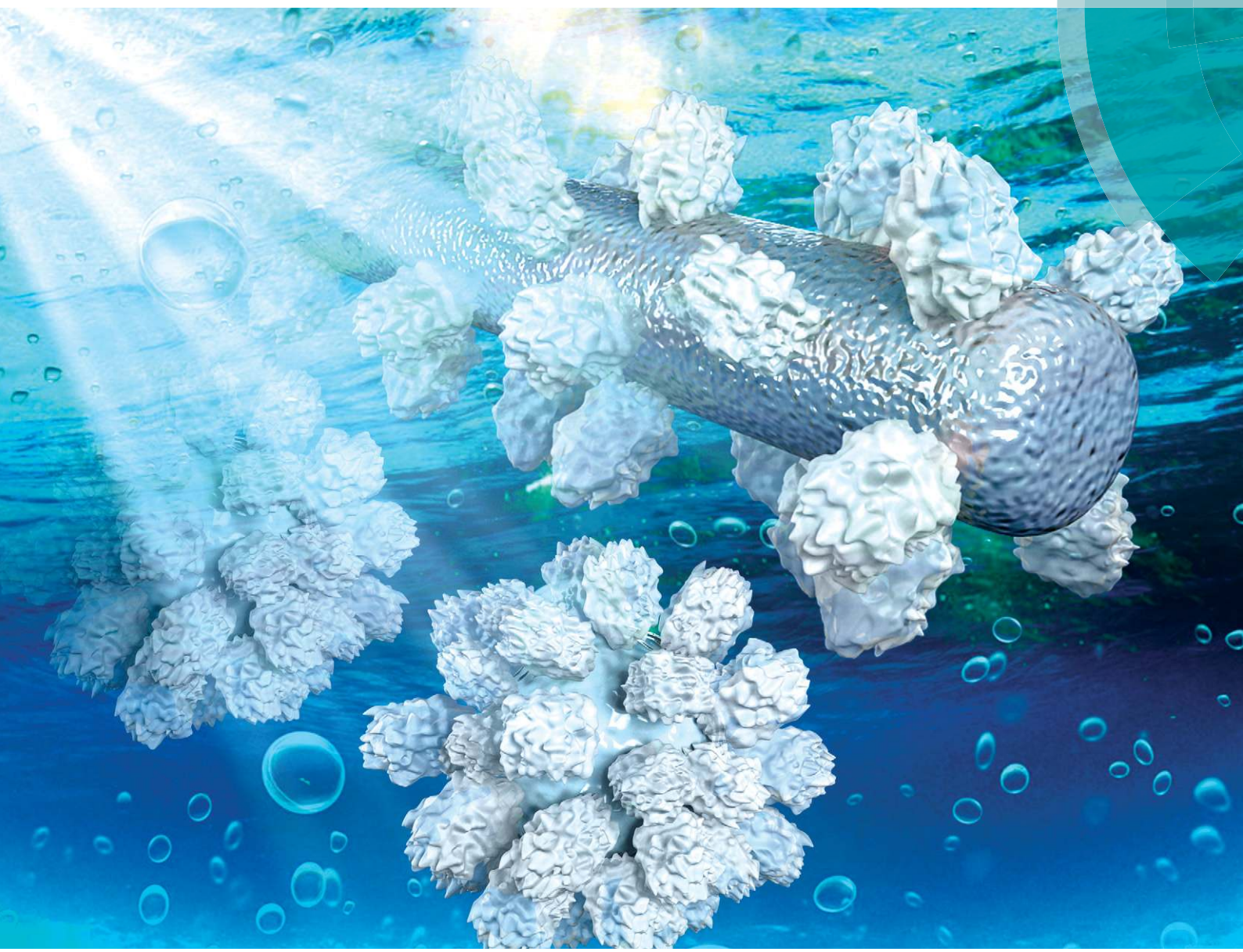

ROYAL SOCIETY OF CHEMISTRY

PAPER
Zhen Li *et al.*
Ambient controlled synthesis of advanced core–shell plasmonic Ag@ZnO photocatalysts

175 YEARS

CrystEngComm

PAPER

View Article Online
View Journal | View Issue

Cite this: *CrystEngComm*, 2016, **18**, 1713

Ambient controlled synthesis of advanced core–shell plasmonic Ag@ZnO photocatalysts†

Jinyan Xiong,[a] Qiao Sun,[b] Jun Chen,[c] Zhen Li*[ab] and Shixue Dou[a]

Plasmonic Ag@ZnO core–shell hybrids, including hetero-nanowires and hetero-nanoparticles, have been synthesized at room temperature for application in photocatalysis. The morphology, size, crystal structure, and composition of the products were investigated by X-ray diffraction, scanning and transmission electron microscopy, X-ray photoelectron spectroscopy, and ultraviolet-visible spectroscopy. It was found the concentration of $Zn(NO_3)_2{\cdot}6H_2O$ and the amount of water play crucial roles in the formation of Ag@ZnO core–shell hybrids. The resultant Ag@ZnO core–shell hybrids exhibit much higher photocatalytic activity and stability towards degradation of organic contaminants than pure ZnO nanocrystals under solar light irradiation. The one-dimensional (1D) core–shell hetero-nanowires prepared under optimal conditions (*i.e.* 0.6 M $Zn(NO_3)_2{\cdot}6H_2O$ and 14.5 mL water) exhibit the best photocatalytic performance. The drastic enhancement in photocatalytic activity over the Ag@ZnO core–shell hybrids, especially the 1D core–shell hetero-nanowires, could be attributed to the synergistic effects of the surface ZnO and Ag nanowire cores with the surface plasmon resonance and the electron sink effect, as well as the unique 1D core–shell nanostructure for efficient mass transfer. The possible mechanism for degradation of rhodamine B (RhB) under solar light irradiation was discussed. This work provides a very convenient chemical route to prepare stable and highly efficient solar light driven plasmonic core–shell Ag@ZnO photocatalysts for cost-effective water purification.

Received 3rd January 2016,
Accepted 2nd February 2016

DOI: 10.1039/c6ce00013d

www.rsc.org/crystengcomm

Introduction

Semiconductor-based heterogeneous photocatalysis, which allows direct conversion of solar energy into chemical energy *via* a renewable route, could be one of the most viable long-term solutions, with the potential to address the issues of energy shortages and environmental pollution.[1] During the past several decades, construction of heterostructures by combining semiconductors with noble metals has attracted increasing interest due to its very high effectiveness in improving the photocatalytic activity, arising from the combined properties and synergistic interactions of the metallic and semiconducting components.[2] As one of the most extensively studied semiconductor photocatalysts, zinc oxide (ZnO) has certain advantages, such as high photocatalytic activity, abundant natural resources, non-toxicity, and low cost, as well as physical and chemical stability.[3] The inherent limitations of the high rate of electron–hole recombination and very low response in the visible range, however, lead to reduced photocatalytic efficiency and inefficient utilization of sunlight.[2a,3b,4] To enhance the photocatalytic performance with improved light harvesting efficiency and to prolong the life of photogenerated carriers, modifications in ZnO have been explored through its composition with novel plasmonic metals.[5] In particular, considerable attention has been paid to the controlled fabrication of heterostructured photocatalysts composed of ZnO and noble metals, such as composites of ZnO hierarchical nanostructures decorated with various noble metals,[6] mesoporous Ag–ZnO nanocomposites,[4c] nanoparticulate Ag–ZnO hybrids,[7] rod-like Ag–ZnO nanocomposite,[5a,8] core–shell Au–ZnO nanoparticles,[3b,9] and hollow Pt–ZnO core–shell nanocomposite.[3a]

Compared with other noble metals, Ag is more attractive because of its high electrical and thermal conductivity, antibacterial characteristics, low cost, and nontoxicity. Ag nanostructures exhibit a wealth of optical and photoelectrochemical properties directly related to their geometry-dependent surface plasmon resonances, which makes it very popular for

[a] *Institute for Superconducting & Electronic Materials, The University of Wollongong, NSW 2500, Australia. E-mail: zhenl@uow.edu.au; Fax: +61 2 42215731*
[b] *School of Radiation Medicine and Radiation Protection, Collaborative Innovation Center of Radiation Medicine of Jiangsu Higher Education Institutions, Soochow University, 199 Ren Ai Road, Suzhou Industrial Park, Suzhou 215123, China. E-mail: zhenli@suda.edu.cn; Fax: +86 512 65882931; Tel: +86 512 65882931*
[c] *Intelligent Polymer Research Institute, The University of Wollongong, NSW 2500, Australia*

† Electronic supplementary information (ESI) available: Experimental conditions for the synthesis of Ag@ZnO samples; XRD patterns and SEM images of the pure ZnO prepared in the presence of different volumes of water. See DOI: 10.1039/c6ce00013d

fabrication of advanced semiconductor/noble metal nanophotocatalysts.[10] For most ZnO/Ag nanophotocatalysts, Ag nanoparticles were decorated on the ZnO surface, and reports on a core–shell structure with an Ag core were rather scarce, although the configuration of Ag@ZnO can eliminate possible disadvantages by the shielding effect on Ag nanoparticles (*e.g.* decrease in photocatalytic active surfaces and obstruction of the exciting light).[9] Moreover, these Ag core@ZnO shell structures have a controllable chemical composition and chemical stability, and are able to electrically insulate the metal nanoparticles from the reactants and the surrounding medium.[3a,b]

Among the reported syntheses, Ag@ZnO core–shell nanoparticles prepared in *N*,*N*-dimethylformamide showed higher activity towards degradation of 9-phenyl-2,3,7-trihidroxy-6-fluorone (PF) as compared to pure ZnO under ultraviolet (UV) excitation.[11] Subsequently, hierarchical hetero-assemblies made of interwoven Ag core nanowires covered by ZnO branched nanorods were fabricated *via* a solution bottom-up strategy, and they also exhibited enhanced photocatalytic properties under UV light irradiation.[12] Liu and co-workers synthesized worm-like Ag–ZnO core–shell heterostructured composites with the assistance of ultrasonic irradiation, and the heterostructures also showed improved photocatalytic activity towards degradation of rhodamine B (RhB) compared to pure ZnO particles.[13] Nevertheless, the synthesis of these Ag–ZnO core–shell heterostructures involved the use of heating, ultrasonication, toxic solvents, or complicated processes. In addition, the resultant Ag–ZnO heterostructure only showed enhanced photocatalytic activity under irradiation with UV light, which accounts for only 4% of the incoming solar light on the earth, while the largest proportion of solar light (*i.e.* visible light) was not efficiently utilized. It remains a great challenge to develop facile and rational strategies for ambient and controllable fabrication of Ag–ZnO core–shell hybrid nanostructures, which have optimal composition and structure, and exhibit excellent photocatalytic activity under excitation with solar light.

Herein, we report a rapid and simple ambient strategy for controllable synthesis of Ag–ZnO core–shell heterostructures with excellent photocatalytic performance under solar excitation. By fine-tuning the amount of water in the reaction mixture, ZnO shells with different sizes and morphologies coating the Ag cores are easily tailored. The impact of the ZnO morphology, the Ag/ZnO molar ratio, and the Ag core on the photocatalytic property of Ag@ZnO heterostructures has been optimized and discussed. The unique one-dimensional (1D) Ag@ZnO hetero-nanowires prepared from 0.6 M $Zn(NO_3)_2{\cdot}6H_2O$ and 14.5 mL H_2O exhibited the highest photocatalytic activity towards degradation of rhodamine B under solar light irradiation compared to pure ZnO and Ag@ZnO nanoparticles. The enhanced photocatalytic performance of Ag@ZnO hetero-nanowires is attributed to their unique morphology for efficient separation of electron–hole pairs.

Experimental

Experimental methods

Ag nanowires (Ag NWs) were fabricated by a modified polyol process.[10a,c] In a typical synthesis, 10 mL 1,2-propanediol containing PVP40 was loaded into a 25 mL vial and heated with magnetic stirring in an oil bath at 135 °C for 1 h. NaCl was then quickly added, and the stirring was continued for another 5 min, followed by addition of 7 mL of 0.1 M $AgNO_3$ solution. The mixed solution was then heated at 135 °C with magnetic stirring for 1 h, yielding the grey Ag NWs.

Ag nanoparticles (Ag NPs) were prepared by a similar procedure without NaCl.

Core–shell Ag@ZnO hetero-nanowires were synthesized by a simple solution process. Typically, 1 mL of 0.6 M $Zn(NO_3)_2{\cdot}6H_2O$ solution and 14.5 mL Milli-Q water were added into 8 mL freshly prepared Ag NW solution under constant magnetic stirring for 30 min. Then, 0.5 mL of 4.8 M NaOH solution was added into the reaction mixture. The reaction mixture was stirred for 1 h, and then the resultant Ag@ZnO core–shell nanowires were separated by centrifugation, washed with Milli-Q water and absolute ethanol to remove impurities, and then dried at 60 °C (A1). Other samples (A2–A14) were also prepared under the identical conditions by varying the volume of water and concentration of $Zn(NO_3)_2{\cdot}6H_2O$. The detailed experimental parameters are listed in Table S1.†

Core–shell Ag@ZnO hetero-nanoparticles were prepared using a similar approach to that for Ag@ZnO core–shell hetero-nanowires, except that 8 mL of Ag NP solution was added rather than Ag NW solution.

Pure ZnO nanostructures were prepared using a similar procedure to that for Ag@ZnO core–shell hetero-nanowires, except that 1,2-propanediol was added rather than the Ag NW solution.

Characterization

The X-ray diffraction (XRD) measurements were performed on a GBC MMA X-ray diffractometer using Cu $K\alpha_1$ radiation (40 kV). The XRD patterns were recorded from 20° to 80° with a scanning rate of 4° min^{-1}. Scanning electron microscope (SEM) images were collected using a field-emission scanning electron microscope (JSM-7500FA, JEOL) operated at an accelerating voltage of 5 kV. Transmission electron microscope (TEM) images were recorded on a field-emission transmission electron microscope (JEM-2011, JEOL), using an accelerating voltage of 200 kV. Ultraviolet/visible (UV/vis) absorption spectra were collected at room temperature on a UV-3600 (Shimadzu) spectrometer. X-ray photoelectron spectroscopy (XPS) was performed on a VG Scientific ESCALAB 2201XL photoelectron spectrometer with Al Kα X-rays as the excitation source to analyse the samples' elemental composition. Analysis of the XPS data was carried out using the commercial CasaXPS 2.3.15 software package.

Photocatalytic test

Photocatalytic activity of the as-synthesized Ag@ZnO core–shell hybrids was evaluated by the degradation of RhB under irradiation with a LSC-100 Solar Simulator with an AM1.5G filter (Newport). In an experiment, 20 mg photocatalyst was added into 50 mL of 10^{-5} M RhB solution at room temperature. Prior to irradiation, the suspension was stirred in the dark to ensure the establishment of an adsorption–desorption equilibrium between the photocatalyst and the RhB. Then, the solution was exposed to solar light irradiation under magnetic stirring. At each irradiation time interval, 2 mL of the suspension was collected and then centrifuged to remove the photocatalyst. The concentration of RhB was analysed by a Shimadzu UV-3600 spectrophotometer, and the characteristic absorption of RhB at 554 nm was used to evaluate its photocatalytic degradation. All of the measurements were carried out at room temperature.

Results and discussion

The X-ray diffraction (XRD) pattern and typical scanning electron microscopy (SEM) images of pure Ag NWs for A1 are given in the supporting information. Fig. S1A† shows the XRD pattern of the as-synthesized Ag NWs applied for the subsequent heterogrowth of ZnO nanoshells to form Ag@ZnO core–shell nanowires. All diffraction peaks match well with that of standard Ag pattern (JCPDS no. 4-783), indicating the high purity of Ag NWs. Fig. S1B and S1C† show typical SEM images of the as-prepared Ag NWs. It can be clearly seen that as-synthesized Ag NWs possess relatively smooth surface, and have an average diameter of about 100 nm and a length of several micrometers. Fig. 1(A) shows a typical scanning electron microscope (SEM) image of the Ag@ZnO core–shell hetero-nanowires (A1), clearly demonstrating that the surface of the Ag@ZnO core–shell hetero-nanowires is not as smooth as that of the Ag NWs, due to the coating of densely packed ZnO nanoparticles. The enlarged SEM image [Fig. 1(B)] reveals that many ZnO nanoparticles have densely grown on the surfaces of the Ag nanowires. TEM and high resolution TEM (HRTEM) were used to further characterize the Ag@ZnO core–shell hetero-nanowires [Fig. 1(C and D)]. Fig. 1(C) clearly shows an individual Ag@ZnO hetero-nanowire with a rough surface, which consists of an 83 nm Ag core and a ZnO shell. The interface between the Ag nanowire and ZnO nanoparticles is also clearly observed. The HRTEM image in Fig. 1(D) shows lattice fringes of 0.282 nm, which corresponds to ZnO (100).

Furthermore, the distribution of elements in the Ag@ZnO core–shell hetero-nanowires was studied with energy-dispersive X-ray (EDX) elemental mapping [Fig. 1(E)]. The left image in Fig. 1(E) is the area where the elemental mapping was performed. The green, blue, and red colors represent the distributions of silver, zinc, and oxygen, respectively. The presence of the three elements in the nanowires is in agreement with the proposed Ag@ZnO composition. The spatial distribution of the colors verifies the core–shell structure,

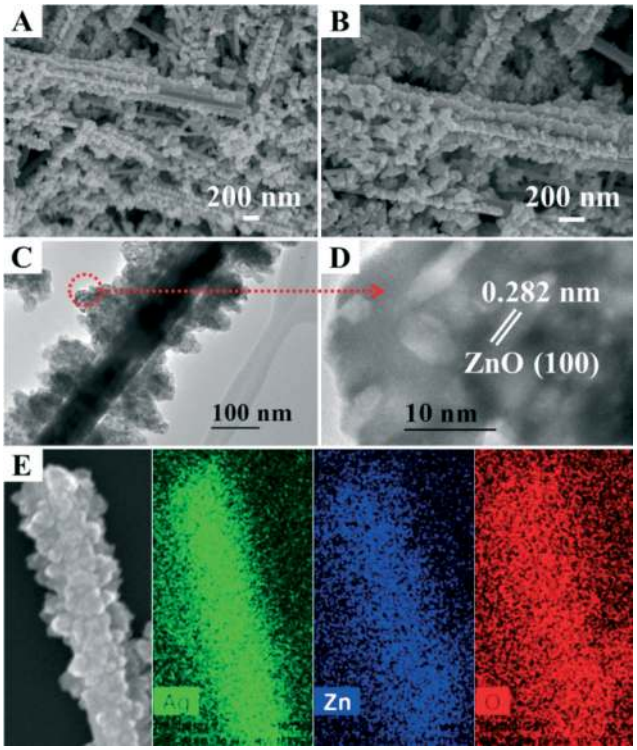

Fig. 1 (A and B) SEM images of the as-prepared Ag@ZnO core–shell hetero-nanowires (A1). (C) TEM image and (D) HRTEM image of an individual Ag@ZnO core–shell hetero-nanowire. (E) EDX elemental mapping analysis of the Ag@ZnO core–shell hetero-nanowires.

where the element Ag is located in the core and the elements Zn and O of ZnO are homogenously distributed throughout the whole NW, showing that the Ag NW core is surrounded with a uniform ZnO shell.

The crystalline structure and optical properties of the as-prepared Ag@ZnO core–shell hetero-nanowires (A1) are shown in Fig. 2. The X-ray diffraction (XRD) pattern is compared with standard patterns of Ag (JCPDS 4-783) and ZnO (JCPDS 5-667) in Fig. 2(A), where every peak can be indexed to Ag or ZnO, supporting the formation of Ag@ZnO core–shell hetero-nanowires. The absence of other impurity peaks indicates the high purity of the core–shell Ag@ZnO hetero-nanowires fabricated by this simple solution process. In addition, the peaks of ZnO are characteristic of a hexagonal structure with a lattice constant a = 3.25 Å. Its relatively weak

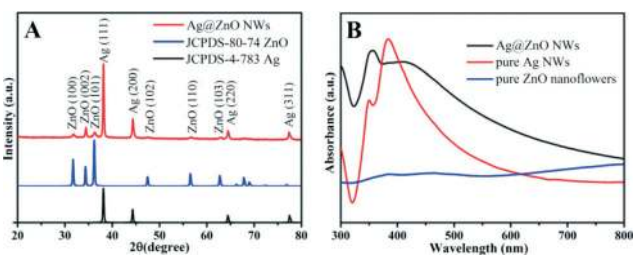

Fig. 2 (A) XRD patterns and (B) UV-vis absorption spectra of as-prepared 1D Ag@ZnO core–shell hetero-nanowires (A1), pure Ag NWs, and pure ZnO nanoflowers in ethanol.

peaks indicate the low crystallinity of the ZnO shell compared to the Ag core.

Ag NWs show intense surface plasmon resonance (SPR) absorption in the visible region, which is highly sensitive to their diameter and length-to-diameter ratio, as well as the optical and electronic properties of their surroundings.[14] The ultraviolet-visible (UV-vis) absorption spectra of pure ZnO nanoflowers, pure Ag NWs, and Ag@ZnO core–shell hetero-nanowires (A1) in ethanol are presented in Fig. 2(B). ZnO nanoflowers exhibit a UV absorption band at ~380 nm. The pure Ag NWs exhibit two absorbance peaks at 350 and 385 nm. The peak at 350 nm could be attributed to the longitudinal mode of the nanowires, similar to that of bulk Ag (ref. 15) or the out-of-plane quadrupole resonance of Ag NWs.[16] The peak at 385 nm is assigned to the transverse plasmon resonance of Ag NWs.[15] Upon the formation of the ZnO shell, the surface plasmon band of the Ag@ZnO core–shell nanowires is distinctly broadened and shows a red-shift compared to that of pure Ag NWs, probably due to a strong interfacial electronic coupling between neighboring ZnO particles and Ag NWs.[13,17] The electron transfer from Ag to ZnO in the Ag@ZnO core–shell nanowires is due to the higher Fermi energy level of Ag than ZnO. This transfer results in deficiency of electrons on the surface of the Ag nanowires, leading to the red-shift in the surface plasmon absorption.[13,18] Similar results for ZnO–Au composites[19] and worm-like Ag/ZnO core–shell heterostructural composites[13] have been reported elsewhere. Their broad absorbance in the UV to visible window clearly demonstrates that our Ag@ZnO nanowires become photoactive in both the UV and the visible light region, which is crucial for full use of sunlight.

X-ray photoelectron spectroscopy (XPS) measurements were carried out to investigate the surface elemental composition and electronic states of Ag@ZnO core–shell hetero-nanowires (A1), as shown in Fig. 3. The survey spectrum in Fig. 3(A) shows the absence of other elements apart from C, Zn, O, and Ag, indicating the high purity of the product, which is consistent with the above XRD and EDX results. High-resolution spectra of Ag, Zn, and O species are shown in Fig. 3(B–D), respectively. The two peaks centred at 367.2 and 373.2 eV are attributed to Ag $3d_{5/2}$ and Ag $3d_{3/2}$, respectively, which are shifted remarkably to lower binding energies compared with those of bulk Ag (Ag $3d_{5/2}$, 368.2 eV; Ag $3d_{3/2}$, 374.2 eV).[3c,20] This result is similar to those obtained from worm-like Ag/ZnO core–shell heterostructured composites,[13] dendrite-like ZnO@Ag heterostructures,[20] Ag–ZnO hetero-structured nanofibers,[3c] and ZnO nanorod/Ag nanoparticle heterostructures.[8,21] The shift of Ag binding energy is mainly attributed to electron transfer from metallic Ag to ZnO crystals (*i.e.*, formation of monovalent Ag). The Fermi levels of the two components equilibrate when the metal nanostructure comes into contact with the semiconductor. When Ag NWs (work function of 4.26 eV) and ZnO nanoparticles (work function of 5.3 eV) become attached together, some electrons are transferred from Ag to ZnO at the interfaces of the ZnO/Ag core–shell heterostructures, resulting in monovalent Ag (*i.e.* Ag^{1+}).[13,20,21] The binding energy of Ag^{1+} is much lower than that of zero-valent Ag (Ag^0). Therefore, the shift of Ag $3d_{5/2}$ and Ag $3d_{3/2}$ to lower binding energies further verifies formation of the ZnO/Ag heterostructure.[13] The Zn 2p peaks shown in Fig. 3(C) have values of about 1021.0 eV ($2p_{3/2}$) and 1043.9 eV ($2p_{1/2}$), confirming the main presence of Zn^{2+} in the sample.[22] The O 1s peak is centred at 530.6 eV [Fig. 3(D)], which is similar to the reported value for ZnO.[22a] All the XPS results further confirm that the core–shell nanowire heterostructure is composed of ZnO and Ag.

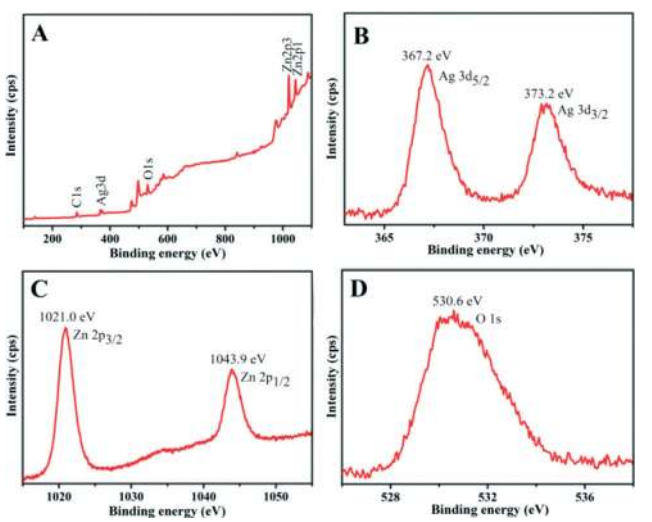

Fig. 3 XPS spectra of the 1D Ag@ZnO core–shell hetero-nanowires (S1): (A) survey-scan spectrum, (B) Ag 3d, (C) Zn 2p, and (D) O 1s.

All the above results confirm our success in obtaining Ag@ZnO core–shell hetero-nanowires through this simple solution approach. It should be noted that the volume of water and the concentration of $Zn(NO_3)_2{\cdot}6H_2O$ play important roles in the formation of Ag@ZnO core–shell hetero-nanowires. As shown in Fig. 4(A–D), when 1.167 mL or 2.5 mL of water is used, the Ag NWs are coated with many very small ZnO nanoparticles (A2 and A3). Increasing the water to 6.5 mL leads to dense ZnO nanoparticles with larger sizes that are deposited on the surfaces of Ag NWs [A4, Fig. 4(E and F)]. Flower petals consisting of nanoparticles are partly coated on the surfaces of the Ag NWs, however, when the volume of water is further increased to 22.5 mL [A5, Fig. 4(G and H)]. Changing the concentration of $Zn(NO_3)_2{\cdot}6H_2O$ could also result in different structured Ag@ZnO nanowires. When the concentration of $Zn(NO_3)_2{\cdot}6H_2O$ is decreased to 0.3 M, flower petals of ZnO assembled from small nanoparticles are partly coated on the surfaces of the Ag NWs (A6), as displayed in Fig. 5(A and B). When the concentration of $Zn(NO_3)_2{\cdot}6H_2O$ is increased to 1.2 M, the ZnO nanoparticles are randomly distributed on the surfaces of Ag NWs [A7, Fig. 5(C and D)]. The above results demonstrate that Ag@ZnO core–shell hetero-nanowires with different morphologies can be achieved by tuning the amount of water or the concentration of $Zn(NO_3)_2{\cdot}6H_2O$.

In order to demonstrate the applicability of our simple method, core–shell Ag@ZnO nanoparticles (NPs) were prepared

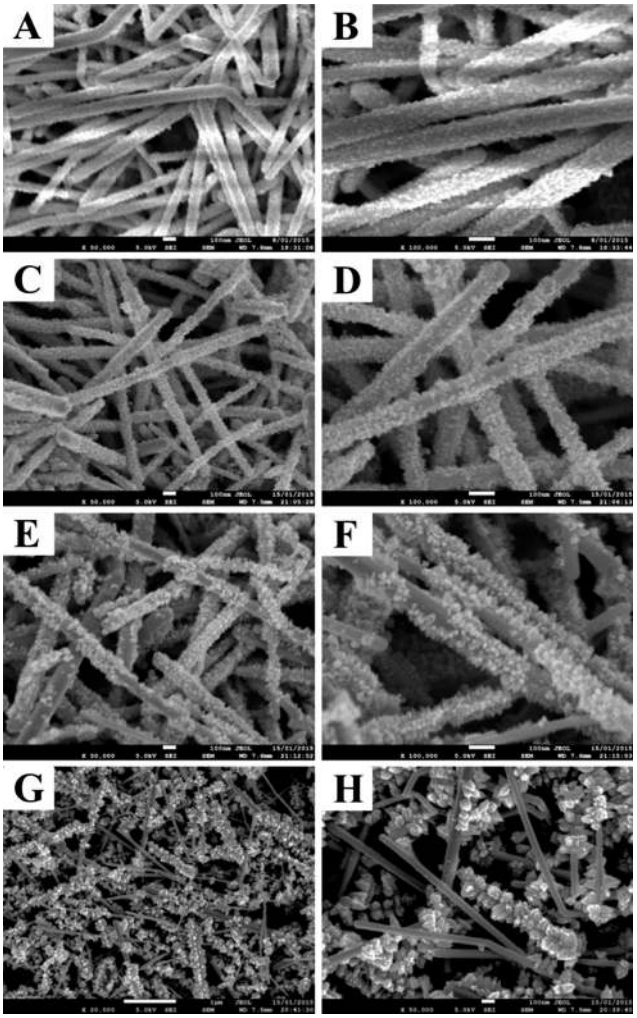

Fig. 4 SEM images of the products (A2–A5) prepared with different volumes of water: (A and B) 1.167 mL, (C and D) 2.5 mL, (E and F) 6.5 mL, and (G and H) 22.5 mL.

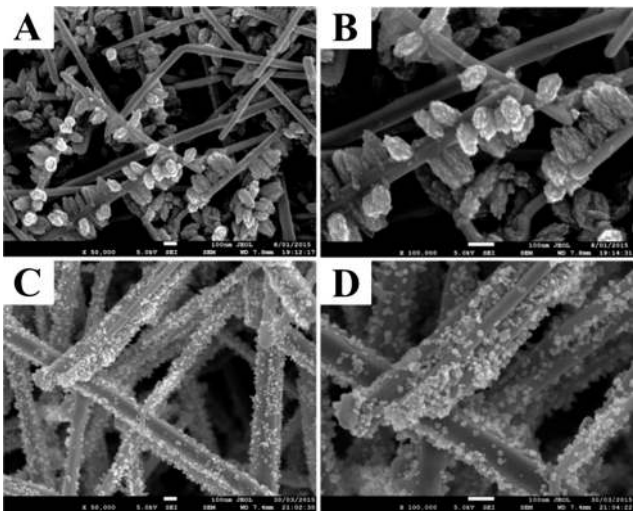

Fig. 5 SEM images of the products (A6 and A7) prepared with different concentrations of $Zn(NO_3)_2{\cdot}6H_2O$: (A and B) 0.3 M, and (C and D) 1.2 M.

under similar conditions by using Ag NPs as seeds. The resultant Ag@ZnO NPs (A8–A12) were examined by XRD and SEM, respectively. The XRD results [Fig. 6(A–E)] clearly reveal that all the diffraction peaks can be indexed to Ag (JCPDS 4-783) and ZnO (JCPDS 5-667), and no other impurity diffraction peaks were observed. The SEM images [Fig. 6(B–O)] show that large quantities of Ag@ZnO NPs with different morphologies were successfully fabricated in the presence of different volumes of water. The particle size and morphology of the ZnO shell can be tailored by changing the volume of water in the system. When the volume of water is 1.167–6.5 mL, the Ag core nanoparticles are packed with small ZnO nanoparticles [A8–A10, Fig. 6(F–K)]. On increasing the volume of water to 14.5 mL, the ZnO nanoparticles aggregate to construct a flower-like structure [A11, Fig. 6(L and M)], and the density of flower petals decreases with further increases in the volume of water [A12, Fig. 6(N and O)].

In addition, the effect of the concentration of $Zn(NO_3)_2{\cdot}6H_2O$ solution was also investigated. When the concentration of $Zn(NO_3)_2{\cdot}6H_2O$ solution is decreased to 0.3 M, the ZnO crystals form a partial coating on the surfaces of Ag NPs, as can be seen from the SEM images [A13, Fig. 7(C and D)]. When the concentration of $Zn(NO_3)_2{\cdot}6H_2O$ solution is increased to 1.2 M, the ZnO nanocrystals cover the surfaces of

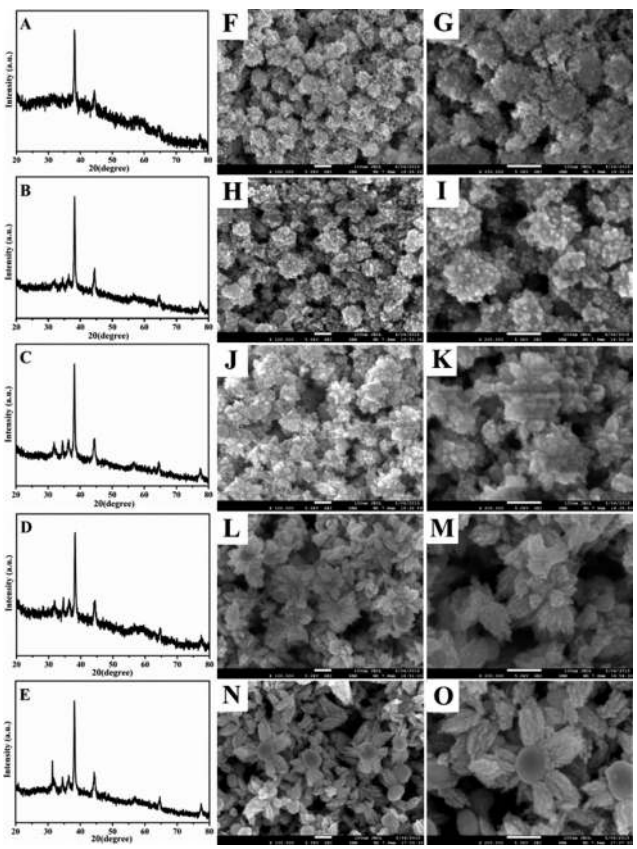

Fig. 6 (A–E) XRD patterns and SEM images of the products (A8–A12) prepared in the presence of different volumes of water: (F and G) 1.167 mL, (H and I) 2.5 mL, (J and K) 6.5 mL, (L and M) 14.5 mL, and (N and O) 22.5 mL.

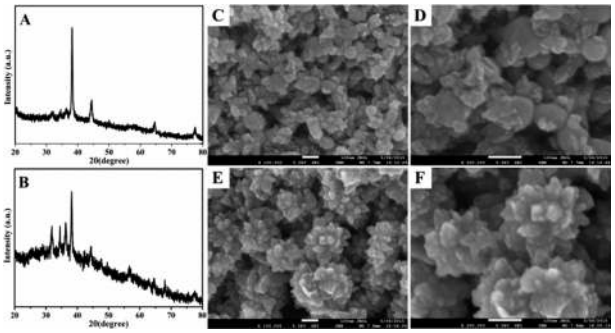

Fig. 7 (A and B) XRD patterns and (C–F) SEM images of the products (A13 and A14) prepared in the presence of different concentrations of $Zn(NO_3)_2{\cdot}6H_2O$ solution: (C and D) 0.3 M, and (E and F) 1.2 M.

the Ag NPs to form a flower-like heterostructure [A14, Fig. 7(E and F)]. These results demonstrate that the final morphology of the Ag@ZnO nanostructures greatly depends on the morphology of the Ag seeds, the volume of water in the system, and the concentration of $Zn(NO_3)_2{\cdot}6H_2O$ solution.

Pure ZnO NPs were also prepared by using 1,2-propanediol instead of Ag NW solution for comparison. The resultant ZnO NPs were examined by XRD and SEM, respectively. The XRD results [Fig. S2(A–E)†] clearly reveal that all the diffraction peaks can be indexed to ZnO (JCPDS 5-667), and no impurity diffraction peaks were observed. The SEM images [Fig. S2(B–O)†] show that large quantities of ZnO nanocrystals with different morphologies were successfully fabricated in the presence of different volumes of water in the system. The size and morphology of ZnO particles is very sensitive to the volume of water, and it can be clearly seen that the ZnO sample comprises very small nanoparticles with a diameter of 8–20 nm when the volume of added water is 1.167 mL [Fig. S2(F and G)†]. When the volume of water is increased to 2.5 mL, the product becomes irregular crystals with diameters of 100–200 nm, assembled from tiny nanoparticles [Fig. S2(H and I)†]. On increasing the volume of water to 6.5 mL, the ZnO nanoparticles aggregate to form flower-like structures with diameters of 600–800 nm [Fig. S2(J and K)†], and the diameter of the flower-like structures increased to ~1 μm on further increasing the volume of water [Fig. S2(L–O)†].

Photoluminescence (PL) spectra were widely used to investigate recombination rate of photogenerated electrons and holes in the photocatalysts during their photocatalysis reaction.[23] Fig. S3† shows the PL spectra of the tested photocatalysts (*i.e.* A1, A11, A2, and pure ZnO) with an excitation wavelength of 325 nm. An UV emission peak centered at around 380 nm and a visible emission in the range of 550–590 nm with high intensity are observed in all photocatalysts. The UV emission corresponds to the near band edge emission of ZnO, and represents the recombination of free excitons through an exciton–exciton collision process.[13,24] The visible emission is attributed to the presence of oxygen related defects and interstitials.[10b] Moreover, The A1 and A11 photocatalysts show a diminished PL intensity in comparison with pure ZnO and A2, indicating that introduction of Ag nanowires and Ag nanoparticles inhibited the recombination of electrons and holes generated in ZnO, which improved the separation of electron–hole pairs and contributed to the enhancement of photocatalytic activity of Ag@ZnO core–shell photocatalysts. Based on the above consideration, all Ag@ZnO core–shell photocatalysts should have better photocatalytic activity than pure ZnO, and A1 sample should be the best photocatalyst among the Ag@ZnO heterostructures as it has the lowest PL emission.

The resultant Ag@ZnO core–shell nanowires and nanoparticles are expected to show higher photocatalytic activity than pure ZnO NPs, due to the plasmonic enhancement of the Ag cores. The performance of the Ag@ZnO NWs (A1–A7) was evaluated by the photodegradation of RhB under solar light irradiation. For comparison, the Ag NWs, Ag@ZnO NPs (A8), and pure ZnO nanoflowers were also tested under identical experimental conditions. If the photodegradation of RhB is considered as a pseudo-first-order reaction;[3c,13,25] its photocatalytic reaction kinetics can be expressed as follows: $C = C_0e^{-kt}$, where k is the degradation rate constant, and C_0 and C are the initial concentration of RhB and the concentration of the pollution at a reaction time of t, which corresponds well to the absorbance of RhB at 554 nm, respectively. Fig. 8(A) shows the photodegradation curves of RhB in the form of $\ln(C_0/C)$ as a function of time, and the k values determined from linear fitting for the as-prepared photocatalysts are listed in Table 1. It can be clearly observed that the degradation of RhB over only Ag NWs under solar light irradiation is negligible.

In contrast, the as-prepared Ag@ZnO core–shell composites and pure ZnO nanoflowers all exhibit excellent photocatalytic performance. In particular, Ag@ZnO core–shell NWs with various morphologies and proportions, and Ag@ZnO core–shell NPs apparently show higher photocatalytic activities than that of the pure ZnO nanoflowers, while the Ag@ZnO core–shell NWs (A1) prepared with 0.6 M $Zn(NO_3)_2{\cdot}6H_2O$ and 14.5 mL water exhibit the highest catalytic activity, which can decolor 99% of RhB within 60 min, with a rate constant (k) of 0.0641 min^{-1}. It should be noted that sample A1 with 1D structured Ag NWs and fusiform ZnO with a high carrier transport property serve as spatially extended active centers to provide direct and fast electron/hole transfer to

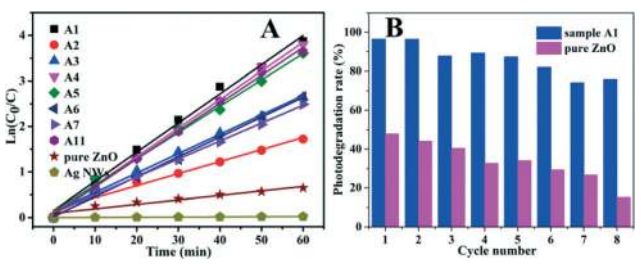

Fig. 8 (A) Rhodamine B degradation curves of $\ln(C_0/C)$ *versus* time for Ag@ZnO heterostructured composite, Ag nanowires, and pure ZnO used as catalyst. (B) Cycling runs in the photocatalytic degradation of RhB in the presence of sample A1 and pure ZnO under solar light irradiation.

Table 1 Reaction rate constant (k) for photocatalytic degradation of RhB under solar light irradiation

Sample	A1	A2	A3	A4	A5
k/min^{-1}	0.0641	0.0265	0.0427	0.0629	0.0578
Sample	A6	A7	A11	Pure ZnO	Ag NWs
k/min^{-1}	0.0437	0.0395	0.0613	0.0098	0.0004

their acceptors (H_2O, O_2, RhB), which increases the chance for RhB dye to be degraded, compared with other 1D structured Ag NWs and ZnO nanoparticles such as samples A2 and A3. A similar kinetics and rate constant value (0.0613 min^{-1}) is also observed with Ag@ZnO core–shell NPs, which is about 6.3 times larger compared to that of the pure ZnO nanoflowers (0.0098 min^{-1}). The results clearly demonstrate that the hetero-growth of ZnO nanoshells on Ag NWs and NPs to build core–shell heterostructures has been proven to be a useful and successful strategy for improving the photocatalytic properties of ZnO crystals, and the photocatalytic performance of the Ag@ZnO core–shell heterostructures can be optimized by tailoring their morphology and proportions.

One main disadvantage of ZnO is its poor stability in degradation of organic pollutants in aqueous solution due to photo-corrosion. To investigate the stability and repeatability of photocatalytic performance in the solar light region, sample A1 and pure ZnO were compared for their ability to degrade RhB in eight repeated cycles, and the results are shown in Fig. 8(B). It was noteworthy that sample A1 exhibited much higher stability than pure ZnO under solar light irradiation. The RhB degradation rate decreased from 48% for the first cycle to 15% for the eighth cycle over pure ZnO photocatalyst, showing poor stability. However, the photocatalytic efficiency was reduced by about 10% and 25% after five cycles and eight cycles, respectively.

It was reported that in the photodegradation of organic pollutants, reactive species such as $^{\bullet}O_2^-$, h^+, e^+, and $^{\bullet}OH$ play the bridge role in photocatalysts under light irradiation,[10a,26] and they could vary with the different photocatalysts.[26b,27] To investigate the photocatalytic mechanism and to understand the better performance of 1D Ag@ZnO core–shell photocatalyst (A1), the effect of scavengers on the degradation of RhB was examined to clarify the contribution of different reactive species during the photocatalysis study. We used p-benzoquinone (PBQ) as O_2^- scavenger,[26a,c,d] triethanolamine (TEOA) as h^+ scavenger,[26b,d] CCl_4 as electron scavenger,[26d] and isopropanol (IPA) as ·OH scavenger.[26c] These scavengers were added into the RhB solution together with the 1D Ag@ZnO core–shell hetero-nanowires before irradiation. As illustrated in Fig. 9, the almost complete inhibition of RhB degradation in the presence of PBQ suggests that $\cdot O_2^-$ is the major reactive species for the photocatalytic degradation of RhB. The dramatic decrease in degradation of RhB in the presence of TEOA demonstrate that h^+ also plays an important role in the photodegradation of RhB over such 1D Ag@ZnO heteronanowires, which was further confirmed by

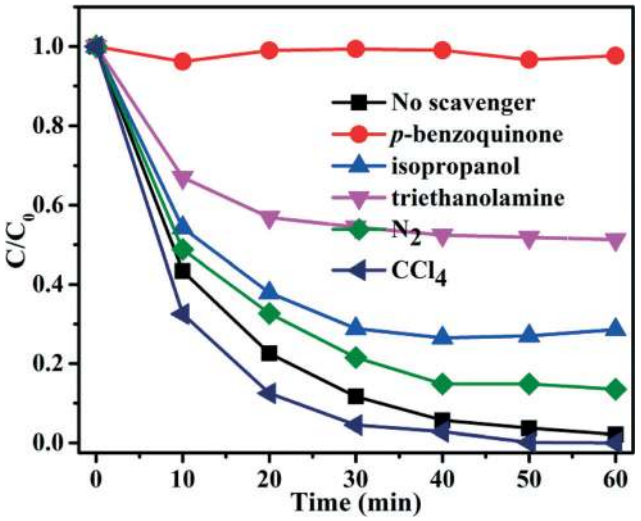

Fig. 9 Photocatalytic degradation of RhB over the 1D Ag@ZnO core–shell hetero-nanowires (A1) in the presence of scavengers.

slight RhB degradation enhancement after adding CCl_4 to capture photogenerated electrons. Meanwhile, the decrease in degradation of RhB arising from the removal of oxygen with bubbling N_2 revealed that molecular oxygen also plays an important role over such 1D Ag@ZnO heteronanowires. This is attributed to the electron trapping role of molecular oxygen, which could produce $^{\bullet}O_2^-$ to inhibit the recombination of electron–hole pairs and leave an excess of holes to oxidize RhB. The elimination of molecular oxygen would diminish the amount of holes and prevent the oxidation of RhB due to the fast recombination of electron–hole pairs. The addition of IPA also indicates that $^{\bullet}OH$ contributes greatly to the degradation of RhB.

As the real photocatalytic mechanism of Ag@ZnO hybrids is very complicated, it is necessary to discuss the band structure of Ag@ZnO heterostructures in detail. The work function of ZnO (5.2 eV) is larger than that of Ag (4.26 eV), which leads to the migration of electrons from Ag to the conduction band (CB) of ZnO to achieve Fermi energy level (E_{fm}) equilibration when coupling of Ag NWs/NPs with ZnO. The transfer of electrons can lead to trapping of charges and increased carrier life. A schematic illustration of the photocatalytic reaction of RhB on Ag@ZnO heterostructures is presented in Scheme 1. For photocatalysis under solar light irradiation, the enhancement in both the UV region and the visible light region should be considered, which may be ascribed to the synergistic effects of Ag NWs/NPs and surface ZnO. As evidenced by the SEM and TEM images, there are clear interfaces between Ag NWs and ZnO nanoparticles, which can effectively suppress the recombination rate of electron–hole pairs.

The enhanced photocatalytic performance in the UV region was attributed to the formation of Schottky barriers at the metal–semiconductor interface between the Ag NW/NP core and the ZnO nanoparticle shell, which facilitates the capture and quick transfer of photoexcited electrons from the ZnO nanoshells to the Ag NWs/NPs under solar light

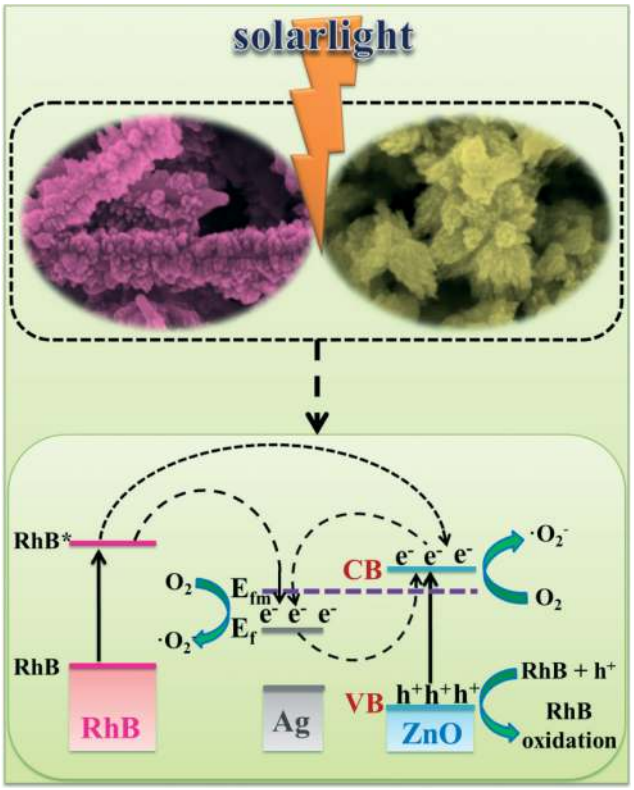

Scheme 1 Schematic illustration of the transfer of photogenerated electron–hole pairs in the Ag@ZnO core–shell NWs/NPs under solar light irradiation.

irradiation.[5a] When the Ag@ZnO core–shell heterojunctions are irradiated by UV light, electrons (e^-) in the valence band (VB) can be excited to the CB with simultaneous generation of the same amount of holes (h^+) in the VB. As presented in Scheme 1, the bottom energy level of the CB of ZnO is higher than the E_F of the Ag/ZnO heterostructures, so that photoexcited electrons can transfer rapidly from ZnO particles to Ag nanowires, driven by the potential energy. Ag NWs/NPs, acting as electron sinks, not only reduce the recombination of photoinduced electrons and holes but also prolong the lifetime of photogenerated pairs. Subsequently, the electrons accumulated in the Ag NWs/NPs or the conduction band of ZnO are transferred to O_2 molecules to produce superoxide radical anions ($^{\cdot}O_2^-$) through multiple-electron reduction reactions to decompose organic pollutant.[3c,28] Accumulation of the photoinduced holes in the valence band of the ZnO nanoshells leads to the production of the hydroxyl radical ($^{\cdot}OH$) at the surface, which is responsible for the oxidation decomposition of the RhB molecules.[3c] Both the sensitizing property of the dye and the electron scavenging ability of silver together contribute to the interfacial charge transfer process to utilize the photoexcited electrons, as well as the VB holes, to form these active oxygen species.[21] In addition, the defects at the Ag@ZnO interface have also been demonstrated to suppress the charge recombination by transferring the photogenerated electrons to the dye in solution.[8]

For the enhancement in the visible light region, the adsorbed RhB would also be photoactivated by the visible light, so that electrons can transfer from the singlet excited RhB (RhB*) to the conduction band (CB) of ZnO, Ag NWs/NPs, and the shallow trap levels in the band gap of ZnO.[5a,21,29] The electrons on the ZnO surface are subsequently trapped by the Ag NWs/NPs, which separates the $RhB^{\cdot+}$ and the electrons, preventing the recombination process.[30] Moreover, the surface plasmon resonance of Ag NWs/NPs excited by the solar light improves the excitation of surface electrons and the transfer of interfacial electrons.[5a] Upon irradiation with visible light, the electrons in E_{fm} were injected quickly into the conduction band (CB) of ZnO *via* a surface phonon resonance (SPR) mechanism, leaving behind holes on the metal surface. Separated electrons might then be consumed by the dissolved oxygen to produce various reactive oxidative species, thus promoting photocatalysis under visible light irradiation.[5a,31]

The unique 1D Ag@ZnO core–shell NWs are expected to have excellent electron conductivity and mobility. The metal nanowires with a high carrier transport property serve as spatially extended catalyzing centres, which can facilitate fast and long-distance electron transport, and the fast transfer of photoinduced electrons and holes over the Ag NWs and ZnO nanoshells suppresses the recombination of electron–hole pairs, which is favorable for increasing the chances for RhB to be degraded, compared with Ag@ZnO core–shell nanoparticles. Furthermore, the high length-to-diameter ratio of the 1D metal-core@semiconductor-shell hetero-nanostructures may remarkably enhance the light absorption, trapping, and scattering through a local field enhancement effect of plasmonic Ag NWs, and thus increase the quantity of photogenerated electrons and holes available to participate in the photocatalytic reactions, leading to an enhanced photocatalytic property of the ZnO. It should be noted, however, that the photocatalytic mechanism over such Ag@ZnO core–shell NWs/NPs is still not completely understood, and a more detailed study is still underway.

Conclusions

In summary, plasmonic Ag@ZnO core–shell hybrids, including hetero-nanowires and hetero-nanoparticles, have been fabricated by a facile solution process at room temperature. The resulting unique heterostructures exhibit greater plasmonic enhancement of photocatalytic activity in RhB oxidizing than pure ZnO under solar light irradiation. The photocatalytic activity and cycling stability of the 1D core–shell hetero-nanowires prepared under optimal conditions is better than that of pure ZnO, which can be attributed to the efficient separation of electron–hole pairs in such 1D Ag@ZnO hetero-nanowires. Such rational design and fabrication of metal-core@semiconductor-shell architectures with hetero-nanowires and hetero-nanoparticles may hold great potential in solar energy utilization.

Acknowledgements

The authors gratefully acknowledge financial support from the Australian Research Council (ARC) through the Discovery Projects DP 130102274 and DP130102699, and from ISEM at UOW, Jiangsu Provincial Key Laboratory of Radiation Medicine and Protection, the Priority Academic Program Development of Jiangsu Higher Education Institutions (PAPD) at Soochow University. The authors also acknowledge the use of the facilities in the UOW Electron Microscopy Centre, with particular thanks to Chao Han, and Australian Nantional Fabrication Facility (ANFF)-Materials node for facility access. They also thank Dr. Tania Silver for critical reading of the manuscript.

Notes and references

1 (*a*) H. Wang, L. Zhang, Z. Chen, J. Hu, S. Li, Z. Wang, J. Liu and X. Wang, *Chem. Soc. Rev.*, 2014, **43**, 5234; (*b*) J. Ran, J. Zhang, J. Yu, M. Jaroniec and S. Z. Qiao, *Chem. Soc. Rev.*, 2014, **43**, 7787; (*c*) J. Xiong, C. Han, Z. Li and S. Dou, *Sci. Bull.*, 2015, **60**, 2083.

2 (*a*) S. T. Kochuveedu, Y. H. Jang and D. H. Kim, *Chem. Soc. Rev.*, 2013, **42**, 8467; (*b*) C.-T. Dinh, H. Yen, F. Kleitz and T.-O. Do, *Angew. Chem., Int. Ed.*, 2014, **53**, 6618.

3 (*a*) C. Yu, K. Yang, Y. Xie, Q. Fan, J. C. Yu, Q. Shu and C. Wang, *Nanoscale*, 2013, **5**, 2142; (*b*) M. Misra, P. Kapur and M. L. Singla, *Appl. Catal., B*, 2014, **150–151**, 605; (*c*) D. Lin, H. Wu, R. Zhang and W. Pan, *Chem. Mater.*, 2009, **21**, 3479; (*d*) A. McLaren, T. Valdes-Solis, G. Li and S. C. Tsang, *J. Am. Chem. Soc.*, 2009, **131**, 12540; (*e*) Y. Lai, M. Meng, Y. Yu, X. Wang and T. Ding, *Appl. Catal., B*, 2011, **105**, 335; (*f*) Y. Bai, H. Yu, Z. Li, R. Amal, G. Q. (Max) Lu and L. Wang, *Adv. Mater.*, 2012, **24**, 5850.

4 (*a*) F. Zhang, Y. Ding, Y. Zhang, X. Zhang and Z. L. Wang, *ACS Nano*, 2012, **6**, 9229; (*b*) W.-j. Sun, J. Li, G. Mele, Z.-q. Zhang and F.-x. Zhang, *J. Mol. Catal. A: Chem.*, 2013, **366**, 84; (*c*) T. Liu, B. Li, Y. Hao, F. Han, L. Zhang and L. Hu, *Appl. Catal., B*, 2015, **165**, 378.

5 (*a*) Q. Deng, X. Duan, D. H. L. Ng, H. Tang, Y. Yang, M. Kong, Z. Wu, W. Cai and G. Wang, *ACS Appl. Mater. Interfaces*, 2012, **4**, 6030; (*b*) Y. Wei, J. Kong, L. Yang, L. Ke, H. R. Tan, H. Liu, Y. Huang, X. W. Sun, X. Lu and H. Du, *J. Mater. Chem. A*, 2013, **1**, 5045; (*c*) X. Liu, M.-H. Liu, Y.-C. Luo, C.-Y. Mou, S. D. Lin, H. Cheng, J.-M. Chen, J.-F. Lee and T.-S. Lin, *J. Am. Chem. Soc.*, 2012, **134**, 10251; (*d*) F. Liao, Y. Huang, J. Ge, W. Zheng, K. Tedsree, P. Collier, X. Hong and S. C. Tsang, *Angew. Chem., Int. Ed.*, 2011, **50**, 2162; (*e*) Z. Cheng, X. Zhan, F. Wang, Q. Wang, K. Xu, Q. Liu, C. Jiang, Z. Wang and J. He, *RSC Adv.*, 2015, **5**, 81723; (*f*) X. Zhan, Y. Bao, F. Wang, Q. Wang, Z. Cheng, Z. Wang, K. Xu, Z. Fang and J. He, *Appl. Phys. Lett.*, 2015, **106**, 123904; (*g*) M. Macias-Montero, R. J. Peláez, V. J. Rico, Z. Saghi, P. Midgley, C. N. Afonso, A. R. González-Elipe and A. Borras, *ACS Appl. Mater. Interfaces*, 2015, **7**, 2331.

6 (*a*) M. Ahmad, S. Yingying, A. Nisar, H. Sun, W. Shen, M. Wei and J. Zhu, *J. Mater. Chem.*, 2011, **21**, 7723; (*b*) M. N. Tahir, F. Natalio, M. A. Cambaz, M. Panthofer, R. Branscheid, U. Kolb and W. Tremel, *Nanoscale*, 2013, **5**, 9944; (*c*) Y. Chen, D. Zeng, K. Zhang, A. Lu, L. Wang and D.-L. Peng, *Nanoscale*, 2014, **6**, 874; (*d*) M. Wu, W.-J. Chen, Y.-H. Shen, F.-Z. Huang, C.-H. Li and S.-K. Li, *ACS Appl. Mater. Interfaces*, 2014, **6**, 15052; (*e*) S. Kuriakose, V. Choudhary, B. Satpati and S. Mohapatra, *Phys. Chem. Chem. Phys.*, 2014, **16**, 17560; (*f*) Y. Jin, J. Xi, Z. Zhang, J. Xiao, F. Xiao, L. Qian and S. Wang, *Nanoscale*, 2015, **7**, 5510; (*g*) Z. Cheng, M. Yu, G. Yang and L. Kang, *CrystEngComm*, 2015, **17**, 1765.

7 E. Mosquera, C. Rojas-Michea, M. Morel, F. Gracia, V. Fuenzalida and R. A. Zárate, *Appl. Surf. Sci.*, 2015, **347**, 561.

8 Y. Zheng, L. Zheng, Y. Zhan, X. Lin, Q. Zheng and K. Wei, *Inorg. Chem.*, 2007, **46**, 6980.

9 T. Jiang, X. Qin, Y. Sun and M. Yu, *RSC Adv.*, 2015, **5**, 65595.

10 (*a*) J. Xiong, Z. Li, J. Chen, S. Zhang, L. Wang and S. Dou, *ACS Appl. Mater. Interfaces*, 2014, **6**, 15716; (*b*) V. P. Dinesh, P. Biji, A. Ashok, S. K. Dhara, M. Kamruddin, A. K. Tyagi and B. Raj, *RSC Adv.*, 2014, **4**, 58930; (*c*) J. Xiong, C. Han, W. Li, Q. Sun, J. Chen, S. Chou, Z. Li and S. Dou, *CrystEngComm*, 2016, **18**, 930.

11 M. E. Aguirre, H. B. Rodríguez, E. San Román, A. Feldhoff and M. A. Grela, *J. Phys. Chem. C*, 2011, **115**, 24967.

12 S. Wang, Y. Yu, Y. Zuo, C. Li, J. Yang and C. Lu, *Nanoscale*, 2012, **4**, 5895.

13 H. R. Liu, G. X. Shao, J. F. Zhao, Z. X. Zhang, Y. Zhang, J. Liang, X. G. Liu, H. S. Jia and B. S. Xu, *J. Phys. Chem. C*, 2012, **116**, 16182.

14 (*a*) J. Li, S. K. Cushing, J. Bright, F. Meng, T. R. Senty, P. Zheng, A. D. Bristow and N. Wu, *ACS Catal.*, 2013, **3**, 47; (*b*) A. Callegari, D. Tonti and M. Chergui, *Nano Lett.*, 2003, **3**, 1565; (*c*) R. Jin, Y. Cao, C. A. Mirkin, K. L. Kelly, G. C. Schatz and J. G. Zheng, *Science*, 2001, **294**, 1901; (*d*) P. Mulvaney, *Langmuir*, 1996, **12**, 788.

15 (*a*) P. Ramasamy, D.-M. Seo, S.-H. Kim and J. Kim, *J. Mater. Chem.*, 2012, **22**, 11651; (*b*) Z. Wang, J. Liu, X. Chen, J. Wan and Y. Qian, *Chem. – Eur. J.*, 2005, **11**, 160; (*c*) Y. Sun, B. Gates, B. Mayers and Y. Xia, *Nano Lett.*, 2002, **2**, 165.

16 (*a*) S. Chen and D. L. Carroll, *Nano Lett.*, 2002, **2**, 1003; (*b*) R. Jin, Y. Charles Cao, E. Hao, G. S. Metraux, G. C. Schatz and C. A. Mirkin, *Nature*, 2003, **425**, 487; (*c*) Y. Gao, L. Song, P. Jiang, L. F. Liu, X. Q. Yan, Z. P. Zhou, D. F. Liu, J. X. Wang, H. J. Yuan, Z. X. Zhang, X. W. Zhao, X. Y. Dou, W. Y. Zhou, G. Wang, S. S. Xie, H. Y. Chen and J. Q. Li, *J. Cryst. Growth*, 2005, **276**, 606.

17 (*a*) F. Li, Y. Yuan, J. Luo, Q. Qin, J. Wu, Z. Li and X. Huang, *Appl. Surf. Sci.*, 2010, **256**, 6076; (*b*) L. Yongchun, L. Yanhong, W. Dejun, W. Lingling, X. Tengfeng and J. Tengfei, *J. Phys. D: Appl. Phys.*, 2011, **44**, 315502.

18 X. Wang, X. Kong, Y. Yu and H. Zhang, *J. Phys. Chem. C*, 2007, **111**, 3836.

19 K. K. Haldar, T. Sen and A. Patra, *J. Phys. Chem. C*, 2008, **112**, 11650.

20 C. Gu, C. Cheng, H. Huang, T. Wong, N. Wang and T.-Y. Zhang, *Cryst. Growth Des.*, 2009, **9**, 3278.

21 Z. Wu, C. Xu, Y. Wu, H. Yu, Y. Tao, H. Wan and F. Gao, *CrystEngComm*, 2013, **15**, 5994.
22 (*a*) D.-M. Tang, G. Liu, F. Li, J. Tan, C. Liu, G. Q. Lu and H.-M. Cheng, *J. Phys. Chem. C*, 2009, **113**, 11035; (*b*) V. Vamathevan, R. Amal, D. Beydoun, G. Low and S. McEvoy, *J. Photochem. Photobiol., A*, 2002, **148**, 233.
23 (*a*) H. Li, Y. Sun, B. Cai, S. Gan, D. Han, L. Niu and T. Wu, *Appl. Catal., B*, 2015, **170–171**, 206; (*b*) X. Li, S. Fang, L. Ge, C. Han, P. Qiu and W. Liu, *Appl. Catal., B*, 2015, **176–177**, 62.
24 T. Sun, J. Qiu and C. Liang, *J. Phys. Chem. C*, 2008, **112**, 715.
25 Q. Wan, T. H. Wang and J. C. Zhao, *Appl. Phys. Lett.*, 2005, **87**, 083105.
26 (*a*) C. Yu, G. Li, S. Kumar, K. Yang and R. Jin, *Adv. Mater.*, 2014, **26**, 892; (*b*) Q. Yuan, L. Chen, M. Xiong, J. He, S.-L. Luo, C.-T. Au and S.-F. Yin, *Chem. Eng. J.*, 2014, **255**, 394; (*c*) Y. He, L. Zhang, B. Teng and M. Fan, *Environ. Sci. Technol.*, 2015, **49**, 649; (*d*) X. Ding, K. Zhao and L. Zhang, *Environ. Sci. Technol.*, 2014, **48**, 5823.
27 L. Chen, R. Huang, S.-F. Yin, S.-L. Luo and C.-T. Au, *Chem. Eng. J.*, 2012, **193–194**, 123.
28 J. Yu, J. Xiong, B. Cheng and S. Liu, *Appl. Catal., B*, 2005, **60**, 211.
29 R. Georgekutty, M. K. Seery and S. C. Pillai, *J. Phys. Chem. C*, 2008, **112**, 13563.
30 Z. Xiong, L. L. Zhang, J. Ma and X. S. Zhao, *Chem. Commun.*, 2010, **46**, 6099.
31 J. Ryu and W. Choi, *Environ. Sci. Technol.*, 2004, **38**, 2928.

